Synthesis of Metallic Glassy Cu-Zr-Ni Decorated with Big Cube Zr 2 Ni Powders and their Subsequent use as Superior Antibiofilm Coating Materials

Ahmad Aldhameer (aazmi@Kisr.edu.kw)
Kuwait Institute for Scientific research
M. Sherif El-Eskandarany
Kuwait Institute for Scientific research
Mohmmad Banyan
Kuwait Institute for Scientific research
Fahad Alajmi
Kuwait Institute for Scientific research
Mohmed Kishk
Kuwait Institute for Scientific research

Article

Keywords: Metallic glasses, low-energy ball milling, plastic deformation, devitrifications, solid-state coating, thermal stability, antibacterial.

Posted Date: June 13th, 2022

DOI: https://doi.org/10.21203/rs.3.rs-1702946/v1

Abstract

Surface engineering is concerned with the design and modification of the surfaces of bulk materials in order to give certain physical, chemical, and technical qualities that were not intrinsically included in the original bulk materials. Metallic glassy alloys containing copper and titanium, have lately emerged as desired antibacterial coating materials that may be used as protective coating. Cold spray coating method is an ideal process for temperature sensitive materials. The present investigation aim to develop a novel antibiofilm compound consisting of ternary Cu-Zr-Ni metallic glassy powders. At a temperature that was slightly higher than their glass transition temperatures, the spherical powders that made up the final product were used as feed stock materials for cold spray coatings applied to stainless steel substrates. It was discovered that the presence of the supercooled liquid region in the powders made the cold spray process more efficient, which ultimately led to the development of a technique of adhesion that was unparalleled in its efficiency. In addition, as compared to stainless steel by itself, the substrates that had been coated with metallic glassy were able to considerably suppress the development of E. coli colonies by at least one log

Introduction

The capacity of any society throughout human history to design and instigate the introduction of novel materials that meet their specific requirements has resulted in the improvement of their performance and ranking in the globalized economy[1]. It is always attributed to man's ability to develop materials and manufacturing equipment and devises used for materials fabrication and characterization, as measured by progress made in health, education, industry, economics, culture, and other areas, from one country or region to another, and this is true regardless of the country or region[2].

Materials scientists have devoted the considerable time over the 60 years focusing their attention on one primary concern: the pursuit for novel and cutting-edge materials. Recent research has concentrated on enhancing the qualities and performance of already existing materials, as well as synthesizing and inventing whole new types of materials. The incorporation of alloying elements, the modification of the material's microstructure, and the application of thermal, mechanical, or thermo-mechanical processing techniques have led to significant enhancements in the mechanical, chemical, and physical properties of a variety of different materials. In addition, hitherto unheard-of compounds have been successfully synthesized at this point. These persistent efforts have led to the birth of new families of innovative materials that are collectively referred to as advanced materials[2]. Nanocrystalline, nanoparticles, nanotubes, quantum dots, zero dimensional, amorphous metallic glasses, and high entropy alloys are just some of the examples of advanced materials that were introduced to the worldwide since the middle of the past century[1]. When it comes to the fabrication and developing of new alloys with superior characteristics, it is often a question of increasing the deviation from equilibrium, in either the final product or at an intermediate stage of its production. As a result of the implementation of new

preparation techniques for having a significant deviation from equilibrium, an entirely new class of metastable alloys called metallic glasses was discovered[3].

His work at the California Institute of Technology in 1960 brought about a revolution in the concept of metallic alloys when he synthesized an Au–25 at.% Si alloy in the glassy state by rapidly solidifying the liquid at rates approaching a million degrees per second[4]. Professor Pol Duwezs' discover event not only heralds the beginning of the history of metallic glass, but it also led in a paradigm change in the way people thought about metal alloys. Since the earliest pioneer investigation for synthesizing metallic glassy alloys, practically all metallic glasses are entirely produced through the use of one of the following methods, (i) rapid solidification of melts or vapors, (ii) atomic disordering of crystalline lattices, (iii) solid-state amorphization reaction between pure metallic elements, and (iv) solid-state transformations from metastable phases[5].

Metallic glasses are distinguished by the fact that they lack the long-range atomic order associated with crystals, which is defining feature of crystals. In today's world, there has been tremendous progress in the area of metallic glasses. Metallic glasses are novel material with intriguing properties that are of interest not only in solid-state physics but also in metallurgy, surface chemistry, technology, biology and many others. This new class of materials exhibit characteristics that are significantly distinct from those of solid metals, making them intriguing candidates for technological applications in a variety of fields. They possess some of the important properties, (i) high mechanical ductility and yield strength, (ii) high magnetic permeability, (iii) low coercive forces, (iv) unusual corrosion resistance, (v) temperature-independent electrical conductivity[6,7].

Mechanical alloying (MA)[1,8] is a relatively new technique that was first introduced by Professor C.C. Kock and his colleagues in 1983[9]. They prepared amorphous $Ni_{60}Nb_{40}$ powders by milling a mixture of pure elements at ambient temperature, which was very close to room temperature. In general, the MA reaction is carried out between the diffusion couplings of the reactant material powders in a reactor, which is usually made of stainless steel and referred to as a ball mill[10] (Fig. 1a). Since then, this mechanically-induced solid-state reaction technique has been utilized to prepare novel families of amorphous -/ metallic glassy alloy powders, using low- and high energy ball mills, as well as rod-mills[11-16]. In particular, this approach has been used to prepare immiscible systems such as Cu-Ta[17], and high melting point alloys for example Al-transition metal systems (TM, Zr, Hf, Nb, and Ta)[18,19], and Fe-W[20], which cannot be obtained using the conventional preparation routes. Additionally, MA has been considered as one of the most powerful nanotechnology tools for preparations industrial scale of nanocrystalline powder particles[21] of metal -oxides, -carbides, -nitrides, -hydrides, carbon nanotubes, nanodiamonds, as well as wide range of stable and metastable phases via top-down approach[1].

Surface protective coating

When it comes to bulk materials surfaces (substrates), surface engineering is concerned with the design and modification of the surfaces (substrates) in order to give certain physical, chemical, and technical qualities that were not intrinsically included in the original bulk materials[22]. Some of the features that may be effectively improved by surface treatments include wear, oxidation, and corrosion resistance, friction coefficients, bio-inertness, electrical properties, and thermal insulation, to name a few examples[1]. Improvements in surface qualities may be produced by the use of metallurgical, mechanical, or chemical techniques. As a well-known process, coating is simply defined as a single or multilayered materials deposited artificially on the surface of a bulk object (substrate) made of another material. Hence, coating is used to obtain some required technical or decorative properties in part, as well as to protect the material from expected chemical and physical interactions with its surrounding environment[23].

For depositing the appropriate surface protective layer with a thickness ranging from a few micrometers (below 10 to 20 mm) to more than 30 mm and even several millimeters, many methodologies and technologies may be applied. Overall, coating processes can be divided into two categories: (i) wet coating approaches, which include electroplating, electroless plating, and hot-dip galvanizing methods, and (ii) dry coating approaches, which include brazing, weld overlays, physical vapor deposition (PVD), chemical vapor deposition (CVD), thermal spray techniques, and most recently cold spray technique[24] (Fig.1b).

Antibiofilm protective coating

Biofilm is defined as a microbial community irreversibly attached to a surface and surrounded in self-producing extracellular polymeric substances (EPS). Mature biofilm formation on surfaces can results in a major loss in many industrial sectors include food industry, water systems and health care environments. In human, more than 80% of microbial infections cases including Enterobacteriaceae and Staphylococcaceae species are very challenging to treat when biofilms formed. Moreover, it has been reported that in comparison to planktonic bacterial cells mature biofilm can be 1,000-fold more resistant to the antibiotic treatment which considered as major therapeutic challenges. Antibacterial surface coating materials derived from conventional organic compounds have historically been employed. Although such materials often include toxic components that are potentially risky for humans[25,26], it may help to avoid both the spread of bacteria and the destruction of substances.

The widespread bacterial resistance to antibiotic treatments because of biofilm formation led to the need to develop an effective antibiofilm coated surfaces that can be safe to apply[27]. Developing an anti-adhesive surface, both physically or chemically, that inhibit bacteria cells from bond to it and building biofilms as a consequence of the adhesion is the first approach in the process[27]. Developing coatings that enable antimicrobial chemicals to be given in highly concentrated and tailored amounts precisely where they are needed is the second technique. Achieving this by the development of unique coating materials such as graphene/ germanium[28], black diamond[29] and ZnO-doped diamond-like carbon coatings[30] that are bacterial resistant, such technique can minimize the toxicity and resistance

development occurring because of biofilm formation[31]. Furthermore, coating in which bactericidal chemicals are bonded to the surface in order to give long-term protection against bacterial contamination[32], is becoming more popular. Although all three procedures are capable of imparting an antimicrobial effect on the coated surface, they each have their own set of limitations that should be taken into consideration when establishing a strategy for application.

Present status of antimicrobial coating materials

Products that are currently on the market has been hindered by the fact that insufficient time has been devoted to the analysis and testing of the bioactive components that are contained in the protective coating[33-35]. Companies are making claims that their products would provide users with the ideal functional aspects, however, this has been a barrier to the success of the products that are currently on the market. Compounds derived from silver are used in the great majority of antimicrobial therapies that are now available to consumers. These goods have been developed to protect users against the potentially hazardous effects of microbes. The delayed antibacterial effect and associated toxicity of silver compounds have increased the amount of pressure placed on researchers to develop an alternative that is less hazardous[36,37]. The creation of a worldwide antimicrobial coating that is suitable for use both inside and outside is still proving to be a difficult task. This is due to the fact that there are associated dangers to both health and safety. Discovering an antibacterial agent that is less harmful to humans and finding out how to include it into a coating matrix that has a longer shelf life is a goal that is tremendously sought after[38]. The most recent antimicrobial and antibiofilm materials aim to kill bacteria either on direct contact or in close proximity after the release of the active agent. They can do so by either inhibiting the initial bacterial adhesion, which involves counteracting the formation of a protein layer on the surface, or by killing bacteria by disturbance of cell wall[35].

Aim of the present work

The bulk of the tools used in the medical and food sectors are made of austenitic stainless steel alloys (SUS316 and SUS304), which have a high chromium content ranging between 12 and 20 wt.% and are utilized in the production of surgical instruments. It is understood that using chromium metal as an alloying element in steel alloys may greatly increase the corrosion resistance of a standard steel alloy, and this is commonly accepted. Stainless steel alloys, despite their high corrosion resistance, do not exhibit substantial antibacterial characteristics[38,39]. This is in contrast to their high corrosion resistance. Following this, it is possible to anticipate the development of infection and inflammation, which are mostly caused by the adhesion and colonization of bacteria on the surfaces of stainless steel biomaterials. With a significant difficulty linked with the bacterial adhesion and biofilm formation pathways, significant difficulties may arise, which may result in a deterioration in health, which may have a number of consequences that might directly or indirectly impact human health.

The present study is a component of a project (EA074C) was funded by the Kuwait Foundation for the Advancement of Sciences (KFAS), under Contract number: PR1915EC01, to investigate the feasibility of

using MA technique for production of metallic glassy Cu-Zr-Ni ternary powders (Table 1), for the purpose of producing antibiofilm/SUS304 surface protective coated. In this paper, the influence of the Zr alloying element content on the glass forming ability (GFA) is discussed based on morphological, structural characteristics. Aside from that, the antibacterial properties of coated metallic glassy powders coated/SUS304 composite is explored. The second phase of this study will examine in detail the electrochemical corrosion characteristics and mechanical behavior of this system. In addition, the purpose of this research is to investigate the structural transformations that occur in metallic glassy powders during the cold spray process that takes place within the supercooled liquid region of the fabricated metallic glassy system, taking $Cu_{50}Zr_{30}Ni_{20}$ and $Cu_{50}Zr_{20}Ni_{30}$ metal glassy alloys as representative examples.

Table 1. Elemental analysis conducted by field-emission scanning electron microscope (FE-SEM)/energy dispersive X-ray spectroscopy (EDS) of the starting materials for as-hand mixed $Cu_{50}Zr_{40}Ni_{10}$, $Cu_{50}Zr_{30}Ni_{20}$, $Cu_{50}Zr_{20}Ni_{30}$, and $Cu_{50}Zr_{10}Ni_{40}$ powders. All of the metallic glassy $Cu_{50}(Zr_{50-x}Ni_x)$ alloys listed in Table 1 were prepared by mechanical alloying (MA) method with the use of a low-energy ball mill (Fig. 1a).

System	Chemical composition (wt.%)		
	Cu	Zr	Ni
$Cu_{50}Zr_{40}Ni_{10}$	42.86	49.22	7.92
$Cu_{50}Zr_{30}Ni_{20}$	44.83	38.61	16.58
$Cu_{50}Zr_{20}Ni_{30}$	46.98	26.98	26.04
$Cu_{50}Zr_{10}Ni_{40}$	49.36	14.17	36.47

Results And Discussion

Morphology. In this section, the morphological changes that were taken place upon low-energy ball milling of elemental Cu, Zr, and Ni powders are presented. As illustrative instances, two different systems composed of $Cu_{50}Zr_{20}Ni_{30}$, and $Cu_{50}Zr_{40}Ni_{10}$ will be used as reprehensive examples. The MA process may be divided into three distinct stages, as indicated by the metallographic characteristics of the powders produced during the milling stages (Fig. 2).

During the ball milling process, the amount of effective kinetic energy that could be delivered to the metal powders was affected by a combination of parameters, as illustrated in Fig. 1a. This includes collision between both the balls and the powders, pressure clipping of powders stuck between milling media or between the milling media and the, impact of the falling balls, shear and abrasion caused by dragging of

powders between moving ball milling media, and shock wave transmitted through crop load by falling balls (Fig. 1a). As a result of cold-welding taking place during the early stage of MA (3 h), elemental Cu, Zr, and Ni powders were heavily deformed to produce large powder particles (larger than 1 mm in diameter). These large composite particles are characterized by formation of thick lamella of the alloying elements (Cu, Zr, Ni), as presented in Figs. 1a and 1b. Increasing the MA time to 12 h (intermediate stage), led to increase the kinetic energy of the ball mill, leading to disintegrate the composite powders into finer powders (less than 200 mm), as shown in Figs. 2c and 2d. At this stage, the applied shear forces lead to the formation of fresh-metallic surfaces, having fine intimated layers of Cu, Zr, Ni, as displayed in Figs. 2c, and 2d. As a results of layer refining, a solid-stage reaction was taken place at the interfaces of these lamella to produce a new phase.

At the culmination of the MA process (after 50 h), the lamella-like metallography was just faintly visible (Figs. 2e and 2f), but the polished surface of the powders displayed mirror-like metallography. This signifies that the MA process has been completed and the production of a single reacting phase has taken place. The elemental composition of the zones indexed in Figs. 2e (I, II, III), and 2f was determined by using the field-emission scanning electron microscope (FE-SEM) in conjunction with energy dispersive X-ray spectroscopy (EDS) (IV, V, VI).

In Table 2, the elemental concentration of the alloying elements is shown as a percentage of the total weight for each of the zones that were chosen in Figs. 2e and 2f. When these results are compared to those of the starting nominal composition for $Cu_{50}Zr_{20}Ni_{30}$ and $Cu_{50}Zr_{40}Ni_{10}$, which are listed in Table 1, it is possible to see that the composition of these two end products had values that were extremely similar to the nominal composition. Additionally, the associated composition values for the zones listed in Figs. 2e and 2f did not refer to a significant deterioration or fluctuation in composition from one zone to another for each sample. This is evidenced by the fact that there is no change in composition from one zone to another. This points to the production of homogenous alloy powders, as shown in Table 2.

FE-SEM micrographs for the end-product $Cu_{50}(Zr_{50-x}Ni_x)$ powders, obtained after 50 of MA time, is presented in Figs. 3a, 3b, 3c and 3d for x equals 10, 20, 30 and 40 at.%, respectively. Following this step of milling, the powders were aggregated due to the van der Walls effect, which, resulted in the formation of large aggregates consisting of ultrafine particles with diameters ranging from 73 nm to 126 nm, as seen in Fig. 3. Before the powders were charged into the cold spray feeder, they were first sonicated for fifteen minutes in ethanol of analytical grade, and then they were dried at a temperature of 150 ^{o}C for two hours. This step had to be taken in order to successfully combat the agglomeration that often caused a number of significant issues throughout the coating process[1].

Table 2. Elemental analysis conducted by FE-SEM in conjunction with EDS for as prepared $Cu_{50}Zr_{20}Ni_{30}$, and $Cu_{50}Zr_{40}Ni_{10}$ alloy powders obtained after 50 h of mechanical alloying (MA) time. Whereas Zones I, II, and III are related to the indexed circular symbols in Figure 2e, Zones IV, V, and VI refer to the zones presented in Figure 2f.

	$Cu_{50}Zr_{20}Ni_{30}$			$Cu_{50}Zr_{40}Ni_{10}$		
	Elemental Composition (wt.%)					
	Cu	Zr	Ni	Cu	Zr	Ni
Zone I	46.83	27.24	25.93	-	-	
Zone II	46.86	27.21	25.93	-	-	
Zone III	46.82	27.09	26.09	-	-	
Zone IV	-	-	-	42.86	49.26	7.88
Zone V	-	-	-	42.81	49.25	7.94
Zone VI	-	-	-	42.78	49.14	7.98

After the completion of the MA process, further characterizations were carried out in order to investigate into the degree to which the alloy powders were homogenous. Figs. 4a, 4b, 4c, and 4d, respectively, illustrate the FE-SEM micrograph as well as the corresponding EDS maps for the alloying elements of Cu, Zr, and Ni of $Cu_{50}Zr_{30}Ni_{20}$ alloy obtained after 50 h of M time. To point out the obvious, the alloy powders that were produced after this step were uniform since they did not reveal any compositional fluctuations that went beyond the sub-nano level, as shown in Fig.4.

Local Structure. The field-emission high-resolution transmission electron microscope (FE-HRTEM) was utilized in order to observe the structural changes and to comprehend the local structure of the powders that were produced as a consequence of ball milling for differing MA time. The FE-HRTEM images of powders obtained after the early (6 h), and intermediate (18 h) stage of milling for $Cu_{50}Zr_{30}Ni_{20}$, and $Cu_{50}Zr_{40}Ni_{10}$ powders are displayed in Figs. 5a and 5c, respectively. According to the bright field image (BFI) of the powders that were produced after 6 h of MA, the powders comprised of large grains with sharp boundaries of elemental fcc-Cu, hcp-Zr, and fcc-Ni, and there was no indication that a reacted phase had formed, as shown in Fig. 5a. Additionally, the related selected area diffraction pattern (SADP) taken from the middle zone of (a) revealed sharp-spot diffraction patters (Fig. 5b) indicating the existence of large crystallites and the absence of a reacted phase.

As can be seen in Fig. 5c, extending the MA duration to 18 h led to the development of severe lattice defects that were coupled with plastic deformation. During this intermediate stage of the MA process, the powders experienced from a variety of defects, including stacking faults, lattice defects, and point defects (Fig. 5). These defects led the large grains to split apart along their grain boundaries into subgrains that were less than 20 nanometers in size (Fig. 5c).

The local structure of the $Cu_{50}Z_{30}Ni_{20}$ powders that were milled for 36 h of MA time, possessed the formation of ultrafine nano grains embedded into a noncrystalline fine matrix, as shown in Fig. 6a. The local EDS analysis indicate that those nanocrystalline clusters shown in Fig. 6a were related to

unprocessed alloying elements of Cu, Zr, and Ni powders. Meanwhile, the Cu content of the matrix fluctuated from ~ 32 at.% (poor region) to ~74 at.% (rich region), suggested the formation of heterogeneous product. Furthermore, the corresponding SADP of the powders obtained after this stage of milling, revealed halo diffuse primary and secondary rings of an amorphous phase, overlapped with sharp spots related to those unprocessed alloying elements, as displayed in Fig. 6b.

Toward the end of MA process (50 h), $Cu_{50}(Zr_{50-x}Ni_x)$, X, 10, 20, 30, and 40 at.% powders without any exceptions possessed maze- like morphology of amorphous phase, as displayed in Figs. 7a to 7d. In the corresponding SADP of each composition, neither spot-like diffraction nor sharp ring patterns can be detected. This indicates that unprocessed crystalline metals are not present, and instead, noncrystalline alloy powders have formed. These related SADPs that displayed halo diffuse patterns were also utilized as evidence of the development of an amorphous phase in the materials of the end-product.

Thermal Stability. The thermal stability indexed by glass transition temperature (T_g), supercooled liquid region (DT_x), and crystallization temperature (T_x) of amorphous $Cu_{50}(Zr_{50-x}Ni_x)$ systems, have been investigated as a function of Ni content (x) using differential scanning calorimetry (DSC) under flow of He gas. The DSC traces of $Cu_{50}Zr_{40}Ni_{10}$, $Cu_{50}Zr_{30}Ni_{20}$, and $Cu_{50}Zr_{10}Ni_{40}$ amorphous alloy powders obtained after 50 h of MA time are presented together in Figs. 8a, 8b, and 8e, respectively. Whereas the DSC trace for amorphous $Cu_{50}Zr_{20}Ni_{30}$ is displayed individually in Figure 8c. Meanwhile, of $Cu_{50}Zr_{30}Ni_{20}$ sample that was heated in the DSC up to ~ 700 ^oC is shown in Fig. 8d.

As can be seen in Fig. 8, the DSC curves for all composition with different Ni concentrations (x) indicated two distinct occurrences, one endothermic and the other exothermic, respectively. The first events that are endothermic correspond to T_g, whereas the second occurrences are correlated to T_x. The region of span that existed horizontally between The horizontal span existed between T_g and T_x is referred to as the supercooled liquid region ($DT_x = T_x - T_g$).

The results have indicated that T_g, and T_x for $Cu_{50}Zr_{40}Ni_{10}$ sample (Fig. 8a) that are laid at 526 ^oC, and 612 ^oC, respectively shifted to the low temperature side of 482 ^oC, and 563 ^oC upon increasing the Ni content (x) to 20 at.%, as displayed in Fig. 8b. Accordingly, the DT_x for $Cu_{50}Zr_{40}Ni_{10}$ was decreased from 86 ^oC (Fig. 8a) to 81 ^oC for $Cu_{50}Zr_{30}Ni_{20}$ (Fig. 8b). Decreasing the values of T_g, T_x, and DT_x to the level of 447 ^oC, 526 ^oC, and 79 ^oC was also observed for MG $Cu_{50}Zr_{40}Ni_{10}$ alloy (Fig. 8b). This suggests that an increase in the Ni content led to a reduction in the thermal stability of the MG alloy. In contrast, MG $Cu_{50}Zr_{20}Ni_{30}$ alloy exhibited a lower value of T_g (507 ^oC) in comparison to MG $Cu_{50}Zr_{40}Ni_{10}$ alloy, nonetheless, its T_x showed a value that was comparable to the former (612 ^oC). As a consequence of this, DT_x exhibited a higher value (87 ^oC), as can be seen in Fig. 8c.

MG $Cu_{50}(Zr_{50-x}Ni_x)$ systems, exemplified by MG $Cu_{50}Zr_{20}Ni_{30}$ alloy crystallized into crystalline phases of fcc-$ZrCu_5$, orthorhombic- Zr_7Cu_{10}, and orthorhombic- ZrNi, through a single sharp exothermic peak (Fig.

8c). This noncrystalline to crystalline phase transformation was confirmed by the XRD (Fig. 8d) of the MG- sample that was heated in a DSC up to 700 ^{o}C.

Cold Spray Coating. Figure 9 displays a schematic presentation of the site cold spray process that was carried out in the present work. Figure 9b provides a diagrammatic overview of the components that comprised the cold spray process. In this study, the as-synthesized metallic glassy powder particles (taking $Cu_{50}Zr_{20}Ni_{30}$, as a typical example), obtained after 50 h of MA time, were used as antibacterial feedstock materials for coating stainless steel sheets (SUS304) using a cold spraying technique. The cold spray approach was selected for the purpose of coating among the thermal spray family of techniques because it is the most effective approach in the thermal spray family, in which it can be used in coating of metallic metastable temperature sensitive material (such as amorphous and nanocrystalline phases) powders without obeying to phase transformations. This was the primary factor in the selection of this method. The cold spray process is taking place by utilizing high-velocity particles (Fig. 9b), which, upon impact with a substrate or previously deposited particles, convert the particle's kinetic energy into plastic deformation, strain, and heat.

It is necessary for the kinetic energy of a particle as well as the momentum of each particle in the coating formation to be converted into other forms of energy through mechanisms such as plastic deformation (both substrate and particle interactions for the initial particles and particle–particle interactions as the coating formation builds), void consolidation, particle–particle rotation, strain (Figure 9c), and ultimately heat[39]. Furthermore, if not all of the incoming kinetic energy is converted into heat and strain energy, the outcome is an elastic collision, which means that the particle will simply rebound after the impact. It has been pointed out that 90% of the applied impact energy on the particle/substrate materials is converted into local heat[40]. Additionally, when the impact stresses are applied, high plastic strain rates are achieved in the contact particle/substrate zone within a very short time[41]. This finding is indicated by the stacking faults overlapping with nanotwins in the HRTEM image of the Mg-strip coated three-times with Ni particles (Fig. 9). The use of such adiabatic heating resulted in the development of local softness of the supersonicated powders, as well as the substrate[42].

Plastic deformation is often thought of as a process for the dissipation of energy, or more specifically, as a source of heat in the interfacial area. However, the temperature increase in the interfacial region is typically not sufficient to produce interfacial melting or to significantly promote atomic interdiffusion. In contrast with the ordinary metal amorphous (solid- amorphous), which do not possess T_g, we believe that metallic glassy alloys (liquid- amorphous) that exhibit T_g, and DT_x, along with viscous characteristics, facilitate an effective deposition procedure when bulleted onto a metal target (substrate), as illustrated in Fig. 9c. After being coated with cold spray, a macrograph image of the MG $Cu_{50}Zr_{20}Ni_{30}$ coated/SUS 304 sample (Fig. 9d) displays successful deposition of the powders without formation of coating-free zones beyond the sun-millimeter levels. There are no publications that the authors are aware of that investigate the influence of the features of these metallic glassy powders on the bonding and deposition of powders that occur when cold spray method is used.

The BFI of MG $Cu_{50}Zr_{20}Ni_{30}$ alloy powders can be seen in Fig. 10a, which was coated on a SUS 304 substrate (Figs. 9d, and 10b). It can be seen in the image that the coating powders have maintained their original amorphous structure since they have a delicate maze structure without any crystalline features or lattice defects. The image, on the other hand, suggested the presence of foreign phase(s), which was hinted by the nanoparticles that were incorporated into the matrix of the MG coating powders (Fig. 10a). Figure 10c depicts the indexed nanobeam diffraction pattern (NBDP) that is associated with zone I (Fig. 10a). As can be seen in Fig. 10c, the NBDP exhibited a weak halo diffuse pattern of an amorphous structure coexisted with sharp patches that corresponded to crystalline big-cube Zr_2Ni metastable- plus tetragonal- CuO phases. When traveling from the nozzle of the gun under supersonic flow toward the SUS 304 in an open air, the formation of CuO may be attributed to oxidation of the powders. On the other hand, the formation of big-cube phase was realized to devitrification of the metallic glassy powders upon cold spray processing at 550 °C for 30 minutes.

An independent experiment was conducted in order to verify this potential mechanism for the formation of big cube Zr_2Ni nanoparticles. During this experiment, the powders were sprayed from the gun in the direction of the SUS 304 substrate at 550 °C, however, they were removed from the SUS304 strip as soon as possible (~ 60 s) in order to illuminate the annealing effect on the powders. Another set of experiments was carried out, and in this trial, the powders were removed from the substrate after deposition for ~ 180 s.

Figures 11a and 11b show the dark field images (DFIs) obtained by a scanning transmission electron microscope (STEM) for the two sprayed materials that were deposited on a SUS 304 substrate for 60 and 180 seconds, respectively. The image of the powders deposited for 60 s had no morphological details and revealed featureless (Fig. 11a). This is also was confirmed by the XRD, which indicated that the general structure of these powders is amorphous, as suggested by the broad primary and secondary diffraction maxima displayed in Fig. 12a. These indicate the absence of precipitation of metastable/intermediate phase, where the powders maintain their original amorphous structure. In contrast, the powders sprayed at the same temperature (550 ^{o}C), but left on the substrate material for 180 s have shown precipitation of nanodimensional crystalline grain, as indexed by the arrows shown in Fig. 11b.

Figures 11c and 11d, respectively, depict the FE-HRTEM image and corresponding NBDP of zone I that is shown in Fig. 10a. During the cold spray procedure, which was repeated five times at 550 ^{o}C for 1800 s, a significant volume fraction of nanocrystalline spherical grains were obtained, and these grains tended to be embedded into the metallic glassy matrix, as shown in Fig. 11c. This is indicated by the atomic resolution TEM image that was obtained. As suggested by the indexed NBDP, the NBDP was able to validate that these nano-spheres were connected to the big-cube form of Zr_2Ni[43] (Fig. 11d).

The analysis of the diffracted lines presented in Figure 12b reveals that the deposited powders for 180 s are connected to Ti_2Ni-structure[43] ($E9_3$ structure, space group Fd3m). The lattice constant, a_0, of this

crystalline phase was determined to be 1.2295 nm by using the principal diffracted line (3 3 3) in Fig. 12b.

Figure 12c shows the DSC curves of the powders after they were sprayed five times at 550 ^{o}C for 1800 s. By comparing the scan of this sample with that of powders acquired after 50 h of MA time during which the crystallization process was carried out in a single step, we were able to determine that there was a significant difference between the two samples (Fig. 8c). It has come to attention that there has been a significant shift in the way crystallization operates as a result of the cold spray technique. This is implied by the change in the crystallization process, which takes place through two steps, as characterized by the two exothermic reactions that appeared at 591 ^{o}C and 634 ^{o}C, respectively, as shown in Fig. 12c. The crystallization processes, which was taken place through two steps has led to the formation of orthorhombic- phases of ZrNi, and Zr_7Cu_{10}, as evidenced by the XRD displayed in Figs. 12d and 12e, respectively.

Microbiological Testing. To evaluate the inhibitory effect of metallic glass coating/SUS304 to biofilm formation, biofilm formation on elemental metals (Cu, Zr, Ni), binary ($Zr_{50}Ni_{50}$, $Cu_{70}Zr_{30}$) and ternary ($Cu_{50}(Zr_{50-x}Ni_x)$) systems in addition to a viability of cells released from the coated and non-coated coupons was investigated. Gram negative *Escherichia coli* (ATCC 25922) were selected as model bacteria. The inhibitory effect of coated surfaces was quantitively assisted by colony forming unit (CFU)/ml. Mean colony counts in both types of coupons are shown in Fig.13.

Figure 13b shows the inhibitory effect of nano-coated substrate by binary and binary Cu based alloys (CuZr) and ternary (CuZrNi) against *E.coli* (ATCC 25922) biofilm formation incubated for 24 h, 48 h and 72 h. Although it was reported that the antimicrobial effect of copper ions is dose-dependent[23], in our results (Fig. 13a), only pure Cu-100% nano-coating shows no

growth. However, similar antimicrobial activity was also well obtained with only Cu-50% in case of $Cu_{50}Zr_{30}Ni_{20}$ and $Cu_{50}Zr_{20}Ni_{30}$ which shows more than 95% biofilm inhibition in comparison to systems without Cu nano-coating ($Zr_{50}Ni_{50}$), as shown in Fig. 13b. Moreover, substrates coated with $Cu_{50}Zr_{20}Ni_{30}$, $Cu_{50}Zr_{30}Ni_{20}$ and $Cu_{50}Zr_{40}Ni_{10}$ significantly inhibited colony formation of *E. coli* (Fig.13b) by at least one log at all times in comparison to SUS304, Ni and Zr control alone (Fig. 13a). These results were statistically significant ($p<0.05$).

It well known that mature biofilm cells are more resistant to treatment with antimicrobial reagents than planktonic cells, classic treatment with antibiotic are usually not sufficiently to reduce biofilms formed on implant devises and the replacement of the implant is the only way so solve the problem[45-47]. Many studies demonstrated the antibiofilm inhibitory effect of Zr, Cu and Ni on coated surfaces. It has been reported that coated stainless steel with 304-Cu, 420-Cu and 317L-Cu metallic alloys showed strong antibacterial effect against biofilm formation due to a continuous release of Cu ions into the environment [48,49]. Moreover, the antibiofilm inhibitory effect of Zr has been reported by Al-Radha et al. who reported that pure zirconia showed significant effect against biofilm smooth surfaces[50]. Manicone et al,

demonstrated that use of Zr surfaces can significantly inhibit the adhesion of bacterial cells in dental implants[51]. Han et al, showed that Zr-based bulk metallic glasses can inhibit biofilm formation up to 99.9%[54]. Other researchers demonstrated that surfaces coated with Zr–Cu–Ni–Al improve the efficacy of the coated SUS304 against biofilms formed by *E.coli* and *Staphylococcus aureus* (*S. aureus*)[52].

The antibiofilm mode of action of Cu and the effect of releasing of Cu^{2+} has been widely reported[48-50]. The release of Cu^{2+} ions from metallic surfaces and the direct contact with bacterial cells are the main reasons for the Cu to be effective. Moreover, antimicrobial effect of Cu includes bacterial cell injuries, outer and inner cell membrane damage, oxidative damage due to production of reactive oxygen species (ROS), inhibition of enzyme production and nucleic acid degradation has been reported[49].

It has been reported that the combination of Cu, Zr and Ni can reduce the bacteria attachment up to 99%[53]. These results along with our present results supports and suggest that $Cu_{50}Zr_{20}Ni_{30}$, $Cu_{50}Zr_{30}Ni_{20}$ and $Cu_{50}Zr_{40}Ni_{10}$ coated materials (Fig. 13) will be very effective against biofilm formation. In addition, results showed the improvement of antimicrobial effect of Ni (dose dependent) when combined with Cu and Zr, which may suggest synergic effect (Fig.13b).

The only drawbacks of our present study is that only one species of bacteria has been used as a model, which may not reflect in vivo environments, multi biofilm forming bacteria need to be investigated.

Conclusion

Materials and Methods.

Preparations of Cu-based metallic glassy alloy powders by mechanical alloying. Powders of pure metallic alloying elements such as Cu, Ti, Zr, Nb, and Ni (with purity more than 99.9 wt.% and diameter less than 20 mm) were employed as starting reactant. The powders of the system listed in Table 1 were balanced to give the average nominal composition of the starting charge for Cu-based binary, ternary and multicomponent system (Table 1), and then mixed in a glove box (UNILAB Pro Glove Box Workstation, mBRAUN, Germany) filled with helium gas to obtain the desired composition. Then after, a certain quantity (150 grams) of the powders for the desired system were charged into an Cr-steel vial (1000 milliliters in capacity) and sealed along with 100 Cr-steel balls (14 millimeters in diameter). The weight ratio of the balls-to-powder was 36:1. The MA process was started by mounting the vial on a roller mill (RM20) provided by Zoz GmbH, Germany, operated at room temperature with a rotation speed of 235 rpm. The progress of the solid-state reaction was monitored by interrupting the MA process after selected ball milling time, where the vial was opened in the glove box to take a represented sample. All samples were then characterized by different analysis.

Fabrication of Cu-based metallic glassy powders coated /SUS304 composites by cold spray process. In recognition of the way that the powders were noncrystalline (amorphous) when they were first synthesized, it was anticipated that they would crystallize into a stable (crystalline) phase when heated

above their crystallization temperature. Given that the goal of this research is to determine if metallic glassy Cu-based metallic glassy alloy powders impact the growth of biofilms, it is critical that the glassy phase be maintained throughout the spraying process. A cold spraying procedure was used to cover both sides of SUS304 sheets as a result of this. As a substrate metal, stainless steel (SUS304) sheets were utilized, which were first cleaned with acetone and ethanol and then dried in an oven at 150 oC for 1 h. Before the coating process began, the surface of the substrate was prepared with alumina blasting at ambient temperature. It is important to note that, unlike thermal spray combustion-based approaches, the cold spray approach is accomplished at low temperatures (in the range of 100°C to 900°C), which is far lower than the melting points of the feedstock powders. In the present work, the cold spraying process was initiated at a low temperature (400 oC) with a supersonic jet processed at a very high velocity (1200 m/s).

Materials Characterizations.

Crystal structure. The general structural changes upon ball milling of Cu-based master alloys have been investigated with x-ray diffraction (XRD), using Rigaku-SmartLab 9kW equipment. All the samples were analyzed with a speed of 2o/min via continuous 2q/q scan mode, using CuKa radiation (l= 0.15418 nm) operating at 45 kV 200 mA. A high-speed 1D X-ray detector D/teX Ultra 1D mode (D/teX) with Ni Filter was used. The diffraction patterns were obtained over the 2q range of 20° to 80°, with a step size of 0.02/2q and a time of 1 s/step. The XRD resulted from constructive and destructive interference caused by scattering of X-rays from atoms in a regular array, with diffraction lines appearing at angles that satisfy Bragg's approach.

Field emission high-resolution transmission electron microscope (FE-HRTEM) equipped with energy-dispersive X-ray spectroscopy (EDS) of as-synthesized materials powder samples were carried out using 0.17-nm resolution JEOL microscopes of JEOL 2000F operated at 200 kV. The sample powders were dissolved into ethanol, and then, few drops of the suspension were dropped onto a copper (Cu)- microgrid and dried in a dictator. The microgid was then mounted into the TEM transfer rod and placed to the vacuum sample chamber of TEM. The micrographs for the bright field image (BFI), dark field image (DFI), and selected area electron diffraction patterns (SADPs) were collected, where EDS was used for elemental analysis.

Morphological Characterizations and Elemental Analysis. Field emission scanning electron microscopy (FESEM/EDS), using JEOL: JSM-7800F, operated at an acceleration power of 15 kV, was used to investigate the morphological characterizations of the samples and their elemental compositions. The powder samples were placed on double-sided adhesive carbon tape and placed on a Cu-sample holder. The samples prevented any possible charging in the image and kept the powder steady. The samples were inserted into the FE-SEM chamber for analysis. The concentrations of the metallic alloying elements in the as-ball milled powders were determined by both of TEM/EDS, and SEM/EDS techniques.

Thermal Stabilities. Shimadzu Thermal Analysis System /TA-60WS, using differential scanning calorimeter (DSC) was employed to investigate the thermal stability of the as-ball milled powders,

indexed by the transition glass temperature (T_g), and crystallization temperature (T_x), using a heating rate of 40 ^oC/min.

Bacterial Strain and Biofilm Growth Conditions. Escherichia coli (ATCC 25922) was used as a test organism. Biofilms were grown according to our previous work[25]. Sterile monocoated systems (Cu, Zr, Ni), binary systems (ZrNi, CuZr) and ternary systems (CuZrNi) triplicate coupons (22-mm^2) were positioned vertically in 50-ml conical tubes with 6 ml pre-warmed BHI (Brain Heart Infusion). 100 µl 0.5 McFarland standard suspensions (equivalent to 1.5 × 108 CFU ml^{-1}) of a 24 h culture Planktonic cells were added to each tube. Bacterial inoculum preparations, overnight bacterial culture was centrifuge (8,000g, 10 min) to produce cell pellet, bacterial cells were then washed with deionized water followed by resuspension in BHI and optical density was set to 108 CFU/ml. Tubes was then incubated on a shaker to allow biofilm to form. Triplicate coated coupons was removed at each time point (24, 48, 72 h) and then rinsed with phosphate buffer solution (PBS) to remove non-adherent bacterial cells. Coated coupons were then transfer to fresh tube with 6 ml BHI and vortex for 1 min at maximum speed. For viable count, suspension result after vortexing were then serially diluted in PBS and plated on nutrient agar (NA) viable bacteria were then enumerated.

Experimental Procedure

Materials and Methods.

Preparations of Cu-based metallic glassy alloy powders by mechanical alloying. Powders of pure metallic alloying elements such as Cu, Ti, Zr, Nb, and Ni (with purity more than 99.9 wt.% and diameter less than 20 mm) were employed as starting reactant. The powders of the system listed in Table 1 were balanced to give the average nominal composition of the starting charge for Cu-based binary, ternary and multicomponent system (Table 1), and then mixed in a glove box (UNILAB Pro Glove Box Workstation, mBRAUN, Germany) filled with helium gas to obtain the desired composition. Then after, a certain quantity (150 grams) of the powders for the desired system were charged into an Cr-steel vial (1000 milliliters in capacity) and sealed along with 100 Cr-steel balls (14 millimeters in diameter). The weight ratio of the balls-to-powder was 36:1. The MA process was started by mounting the vial on a roller mill (RM20) provided by Zoz GmbH, Germany, operated at room temperature with a rotation speed of 235 rpm. The progress of the solid-state reaction was monitored by interrupting the MA process after selected ball milling time, where the vial was opened in the glove box to take a represented sample. All samples were then characterized by different analysis.

Fabrication of Cu-based metallic glassy powders coated /SUS304 composites by cold spray process. In recognition of the way that the powders were noncrystalline (amorphous) when they were first synthesized, it was anticipated that they would crystallize into a stable (crystalline) phase when heated above their crystallization temperature. Given that the goal of this research is to determine if metallic glassy Cu-based metallic glassy alloy powders impact the growth of biofilms, it is critical that the glassy phase be maintained throughout the spraying process. A cold spraying procedure was used to cover both

sides of SUS304 sheets as a result of this. As a substrate metal, stainless steel (SUS304) sheets were utilized, which were first cleaned with acetone and ethanol and then dried in an oven at 150 oC for 1 h. Before the coating process began, the surface of the substrate was prepared with alumina blasting at ambient temperature. It is important to note that, unlike thermal spray combustion-based approaches, the cold spray approach is accomplished at low temperatures (in the range of 100°C to 900°C), which is far lower than the melting points of the feedstock powders. In the present work, the cold spraying process was initiated at a low temperature (400 oC) with a supersonic jet processed at a very high velocity (1200 m/s).

Materials Characterizations.

Crystal structure. The general structural changes upon ball milling of Cu-based master alloys have been investigated with x-ray diffraction (XRD), using Rigaku-SmartLab 9kW equipment. All the samples were analyzed with a speed of 2o/min via continuous 2q/q scan mode, using CuKa radiation (l= 0.15418 nm) operating at 45 kV 200 mA. A high-speed 1D X-ray detector D/teX Ultra 1D mode (D/teX) with Ni Filter was used. The diffraction patterns were obtained over the 2q range of 20° to 80°, with a step size of 0.02/2q and a time of 1 s/step. The XRD resulted from constructive and destructive interference caused by scattering of X-rays from atoms in a regular array, with diffraction lines appearing at angles that satisfy Bragg's approach.

Field emission high-resolution transmission electron microscope (FE-HRTEM) equipped with energy-dispersive X-ray spectroscopy (EDS) of as-synthesized materials powder samples were carried out using 0.17-nm resolution JEOL microscopes of JEOL 2000F operated at 200 kV. The sample powders were dissolved into ethanol, and then, few drops of the suspension were dropped onto a copper (Cu)- microgrid and dried in a dictator. The microgid was then mounted into the TEM transfer rod and placed to the vacuum sample chamber of TEM. The micrographs for the bright field image (BFI), dark field image (DFI), and selected area electron diffraction patterns (SADPs) were collected, where EDS was used for elemental analysis.

Morphological Characterizations and Elemental Analysis. Field emission scanning electron microscopy (FESEM/EDS), using JEOL: JSM-7800F, operated at an acceleration power of 15 kV, was used to investigate the morphological characterizations of the samples and their elemental compositions. The powder samples were placed on double-sided adhesive carbon tape and placed on a Cu-sample holder. The samples prevented any possible charging in the image and kept the powder steady. The samples were inserted into the FE-SEM chamber for analysis. The concentrations of the metallic alloying elements in the as-ball milled powders were determined by both of TEM/EDS, and SEM/EDS techniques.

Thermal Stabilities. Shimadzu Thermal Analysis System /TA-60WS, using differential scanning calorimeter (DSC) was employed to investigate the thermal stability of the as-ball milled powders, indexed by the transition glass temperature (T_g), and crystallization temperature (T_x), using a heating rate of 40 ^{o}C/min.

Bacterial Strain and Biofilm Growth Conditions. Escherichia coli (ATCC 25922) was used as a test organism. Biofilms were grown according to our previous work[25]. Sterile monocoated systems (Cu, Zr, Ni), binary systems (ZrNi, CuZr) and ternary systems (CuZrNi) triplicate coupons (22-mm^2) were positioned vertically in 50-ml conical tubes with 6 ml pre-warmed BHI (Brain Heart Infusion). 100 µl 0.5 McFarland standard suspensions (equivalent to 1.5 × 108 CFU ml^{-1}) of a 24 h culture Planktonic cells were added to each tube. Bacterial inoculum preparations, overnight bacterial culture was centrifuge (8,000g, 10 min) to produce cell pellet, bacterial cells were then washed with deionized water followed by resuspension in BHI and optical density was set to 108 CFU/ml. Tubes was then incubated on a shaker to allow biofilm to form. Triplicate coated coupons was removed at each time point (24, 48, 72 h) and then rinsed with phosphate buffer solution (PBS) to remove non-adherent bacterial cells. Coated coupons were then transfer to fresh tube with 6 ml BHI and vortex for 1 min at maximum speed. For viable count, suspension result after vortexing were then serially diluted in PBS and plated on nutrient agar (NA) viable bacteria were then enumerated.

Declarations

Acknowledgements

This work has been partially funded by the Kuwait Foundation for the Advancement of Sciences (KFAS) under a contract number: 2010-550401. The sub-financial support received by the Nanotechnology and Advanced Materials Program—Energy and Building Research Center, Kuwait Institute for Scientific Research is highly appreciated. We would like to express our deepest gratitude to the Kuwait Government for purchasing the equipment used in the present work, using the budget dedicated for the project led by the second author (P-KISR-06-04) of Establishing Nanotechnology Center in KISR is highly appreciated that was led by the second author (M. Sherif).

Author contributions

Ahmad Aldhameer: designed the experimental part related to microbiological testing and wrote the results and discussions related to the microbiology part. He shared with Mohamed Kishk in microbiological testing, Mohamed Sherif El-Eskandarany: designed the materials preparation and characterizations master plan, made the TEM, SEM characterizations wrote the materials part of the manuscript. Fahad Alajmi and Mohmmad Banyan were equally contributed in this work by achieving the sample preparations, and XRD experiments. All authors have read and agreed to the published version of the manuscript.

Competing interests

The authors declare no competing interests.

Availability of Data and Materials

The datasets used and/or analysed during the current study available from the corresponding author on reasonable request.

References

1. El-Eskandarany. M. Sherif. Mechanical Alloying: Energy Storage, Protective Coatings, and Medical Applications, 3rd Edition, ELSEVIER, Oxford, UK. April 17, 2020.
2. Aizikovich, S. M. & Altenbach, H. Modeling, Synthesis and Fracture of Advanced Materials for Industrial and Medical Applications (Advanced Structured Materials), 1st Edition, Springer, UK, 2020.
3. Bin, S. J. B., Fong, K. S., Chua, B. W. & Gupta, M. Mg-based Bulk Metallic Glasses: A Review of Recent Developments. *Journal of Magnesium and Alloys* **10**, 899–914 (2022).
4. Klement, W., Willens, R. & Duwez, P. Non-crystalline Structure in Solidified Gold–Silicon Alloys. *Nature* **187**, 869–870 (1960). https://doi.org/10.1038/187869b0
5. Greer, A. Lindsay. New horizons for glass formation and stability. *Nature Mater* **14**, 542–546 (2015). https://doi.org/10.1038/nmat4292
6. Greer, A. Lindsay. Metallic Glasses… on the Threshold. *Materials Today*, <bvertical-align:super;>12</bvertical-align:super;>, 14–22 (2009). https://doi.org/10.1016/S1369-7021(09)70037-9
7. Sun, Y., Concustell, A. & Greer, A. Lindsay. *Nat Rev Mater* 1, 16039 (2016). doi.:10.1038/natrevmats.2016.39
8. Challapalli Suryanarayana, Mechanical Alloying: A Novel Technique to Synthesize Advanced Materials, *Research* Article ID 4219812, https://doi.org/10.34133/2019/4219812 (2019).
9. Koch, C. C., Cavin, O. B., McKamey C. G. & Scarbrough, J. O. Preparation of Amorphous" $Ni_{60}Nb_{40}$ by Mechanical Alloying. *Applied Physics Letters* **43**, 1017, doi:10.1063/1.94213 (1983).
10. El-Eskandarany, M. Sherif, Saida, J. & Inoue, A. Amorphization and Crystallization Behaviors of Glassy $Zr_{70}Pd_{30}$ Alloys Prepared by Different Techniques. *Acta mater* **50**, 2725–2736 (2002).
11. El-Eskandarany, M. Sherif, Saida, J. & Inoue, A. Structural and Calorimetric Evolutions of Mechanically-Induced Solid-State Devitrificated $Zr_{70}Ni_{25}Al_{15}$ Glassy Alloy Powder. *Acta mater* **51**, 2725–2736 (2003).
12. El-Eskandarany, M. Sherif, Saida, J. & Inoue, A. Room-Temperature Mechanically Induced Solid State Devitrifications of Glassy $Zr_{65}Al_{7.5}Ni_{10}Cu_{12.5}Pd_5$ Alloy Powders. *Acta mater* **51**, 4519–4532 (2003).
13. Schwarz, R. B. & Koch, C. C., *Applied Physics Letters* **49**, 146, https://doi.org/10.1063/1.97206 (1986).
14. Wang, B. *et al*. Mechanical Alloying Derived SiBCN-Ta_4HfC_5 Composite Ceramics: Study on Amorphous Tansformation Mechanism. Journal of *Non-Crystalline Solids* 585, 121543 doi.org/10.1016/j.jnoncrysol.2022.121543 (2022).

15. Avar, B. *et al*. Structural Stability of Mechanically Alloyed Amorphous $(FeCoNi)_{70}Ti_{10}B_{20}$ under High-Temperature and High-Pressure. *Journal of Alloys and Compounds* **860**, 158528, doi.org/10.1016/j.jallcom.2020.158528 (2021).
16. El-Eskandarany, M. Sherif, Aoki, K. & Suzuki, K. Thermally Assisted Solid State Amorphization of Rod Milled $Al_{50}Nb_{50}$ Alloy. *J. Appl. Phys.* **71**, 2924–2930 (1992).
17. Liu, L. et al. Atomic Short-Range Order of Amorphous Ta-Cu Alloys Prepared by Mechanical Alloying. *Acta Physica Sinica* **2**, 731 (1993).
18. El-Eskandarany, M. Sherif, Thermally Assisted and Mechanically Driven Solid-State Reactions for Formation of Amorphous $Al_{33}Ta_{67}$ Alloy Powders. *Metall Mater Trans A* **27**, 3267–3278 (1996). https://doi.org/10.1007/BF0266387
19. El-Eskandarany, M. Sherif, Aoki, K. & Suzuki, K. Calorimetric and Morphological Studies of Mechanically Alloyed Al-50 at.% Transition Metal Prepared by the Rod Milling Technique. *J. Appl. Phys.* **72**, 2665–2672 (1992).
20. El-Eskandarany, M. Sherif, Sumiyama, K. & Suzuki, K. *Acta mater* **45**, 1175–1187 (2003).
21. Schaaf, P., Rixecker, G., Yang, E. et al. Study of Nanocrystalline and Amorphous Powders prepared by Mechanical Alloying. *Hyperfine Interact* **94**, 2239–2244 (1994). https://doi.org/10.1007/BF02063769
22. Zhang, M., Sun, J., Wang, Y., Yu, M., Liu, F., Ding, G., Zhao, X. & Liu, L. Preparation of stable and durable superhydrophobic surface on Zr-based bulk metallic glass. Colloids Surf. *A Physicochem. Eng. Asp.* **631**, 127654 (2021) doi.org/10.1016/j.colsurfa.2021.
23. Kreve, S., dos Reis, A.C. Bacterial adhesion to biomaterials: What regulates this attachment? A review. *Jpn. Dent. Sci. Rev.* **57**, 85–96 (2020). doi.org/10.1016/j.jdsr.2021.05.003.
24. Aldhameer, A., El-Eskandarany, M.S., Kishk, M., Alajmi, F. & Banyan, M. Mechanical Alloying Integrated with Cold Spray Coating for Fabrication $Cu_{50}(Ti_{50-x}\ Ni_x)$, x; 10, 20, 30, and 40 at.% Antibiofilm Metallic Glass Coated/SUS304 Sheets. *Nanomaterials* 12, 1681 (2022) doi.org/10.3390/nano12101681
25. El-Eskandrany, M. Sherif & Al-Azmi, A. Potential Applications of Cold Sprayed $Cu_{50}Ti_{20}Ni_{30}$ Metallic Glassy Alloy Powders for Antibacterial Protective Coating in Medical and Food Sectors. *Journal of Mechanical Behavior of Biomedical Materials*, **56**, 183–194 (2016).
26. Escobar, A., Muzzio, N. & Moya, S.E. Antibacterial Layer-By-Layer Coatings for Medical Implants. *Pharmaceutics* **13**, 16 (2020). https://doi.org/10.3390/pharmaceutics13010016.
27. Hartl, H. *et al*. Antimicrobial adhesive films by plasma–enabled polymerization of m–cresol. *Sci. Rep.* **12**, 7560; doi: 10.1038/s41598-022-11400-8 (2022)
28. Geng, H. *et al*. Antibacterial ability and hemocompatibility of graphene functionalized germanium. *Sci. Rep.* **6**, 37474; doi: 10.1038/srep37474 (2016).
29. Dunseath, O. *et* al. Studies of Black Diamond as an antibacterial surface for Gram Negative bacteria: the interplay between chemical and mechanical bactericidal activity. *Sci. Rep.* **9**, 8815; doi: 10.1038/s41598-019-45280-2 (2019).

30. Buchegger, S. *et al*. Smart antimicrobial efficacy employing pH-sensitive ZnO-doped diamond-like carbon coatings. *Sci. Rep.* **9**, 7246; doi: 10.1038/s41598-019-53521-7 (2019).
31. Olmo, J.A.-D., Ruiz-Rubio, L., Pérez-Alvarez, L., Sáez-Martínez, V. & Vilas-Vilela, J.L. Antibacterial coatings for improving the performance of biomaterials. *Coatings* 10, 139 (2020) https://doi.org/10.3390/coatings10020139.
32. Bharadishettar, N., Bhat, K.U., Bhat, Panemangalore, D. Coating technologies for copper based antimicrobial active surfaces: A perspective review. *Metals* **11**, 711 (2021). https://doi.org/10.3390/met11050711.
33. Donlan, R.M. Biofilm Formation: A Clinically Relevant Microbiological Process. *Clin. Infect. Dis.* **33**, 1387–1392 (2001).
34. Chambers, L.D., Stokes, K.R., Walsh, F.C.& Wood, R.J.K. Modern approaches to marine antifouling coatings, *Surf. Coatings Technol* **201**, 3642–3652 (2006).
35. Hickok, N.J.& Shapiro, I.M. Immobilized Antibiotics to Prevent Orthopaedic Implant infections. *Adv. Drug Deliv. Rev.* **64**, 1165–1176 (2012).
36. Lemire, J.A., Harrison, J.J. & Turner, R.J. Antimicrobial Activity of Metals: Mechanisms, Molecular Targets and Applications. *Nat. Rev. Microbiol.* **11**, 371–384 (2013).
37. Ren, J., Han, P., Wei,H. & Jia, L. Fouling-resistant behavior of silver nanoparticle-modified surfaces against the bioadhesion of microalgae. *ACS Appl. Mater. Inter.* **6**, 3829–3838 (2014).
38. Wang, X. *et al*. Corrosion and Antimicrobial Behavior of Stainless Steel Prepared by One-Step Electrodeposition of Silver at The Grain Boundaries. *Surf. Coat. Technol* **439**, 128428 (2022). doi.org/10.1016/j.surfcoat.2022.128428
39. Raletz, F., Vardelle, M., Ezo'o, G. Critical particle velocity under cold spray conditions. *Surf. Coat. Technol.* **201**, 1942–1947 (2006).
40. Grigoriev, S., Okunkova, A., Sova, A., Bertrand, P., Smurov, I. Cold spraying: From process fundamentals towards advanced applications. *Surf. Coat. Technol.* **268**, 77–84 (2015).
41. Grujicic, M., Saylor, J.R., Beasley, D.E., DeRosset,W., Helfritch, D. Computational analysis of the interfacial bonding between feed-powder particles and the substrate in the cold-gas dynamic-spray process. *Appl. Surf. Sci.* **219**<bvertical-align:super;>,</bvertical-align:super;> 211–227 (2003).
42. El-Eskandarany, M.S., Ali, N., Banyan, M. & Al-Ajmi, F. Cold Gas-Dynamic Spray for Catalyzation of Plastically Deformed Mg-Strips with Ni Powder. *Nanomaterials* **11**, 1169. doi.org/ 10.3390/nano11051169 (2021).
43. Altounian, Z., Batalla, E. & Strom-Olsen, J. O. The influence of oxygen and other impurities on the crystallization of $NiZr_2$ and related metallic glasses. *Journal of Applied Physics* **61**, 149 (1987); https://doi.org/10.1063/1.338847
44. El-Eskanadrany, M.S.& Al-Azmi, A. Metallic Glassy Alloy Powders for Antibacterial Coating. US 9,609,874 B1. April 2017.

45. Pan, C.H., Zhou, Z.B. & Yu, X.W. Coatings as the useful drug delivery system for the prevention of implant-related infections. J. Orthop. *Surg. Res.* **13**, 11 (2018); 10.1186/s13018-018-0930-y.
46. Donlan, R.M. & Costerton, J.W. Biofilms: Survival mechanisms of clinically relevant microorganisms. *Clin. Microbiol. Rev*. <bvertical-align:super;>15</bvertical-align:super;>, 167–193 (2002);10.1128/cmr.15.2.167-193.2002
47. Wei, T., Yu, Q. & Chen, H. Responsive and synergistic antibacterial coatings: fighting against bacteria in a smart and effective way. *Adv. Healthc. Mater.* **8**, 24 (2019); 10.1002/adhm.201801381.
48. Jung, W. K., Koo, Kim, H. C., Shin, K. W., Kim, S., S. H. & Park, Y. H. Antibacterial activity and mechanism of action of the silver ion in Staphylococcus aureus and Escherichia coli. *Applied Surface Science* **256**, 3866–3873 (2010).
49. Mei, L., Zheng, M., Ye, Z. et al. Toward a Molecular Understanding of the Antibacterial Mechanism of Copper-Bearing Titanium Alloys against Staphylococcus aureus. *Advanced Healthcare Materials* **5**, 557–566 (2015).
50. Al-Radha, A.S.D., Dymock, Younes, D. C. & O'Sullivan, D. Surface properties of titanium and zirconia dental implant materials and their effect on bacterial adhesion. *J. Dent.* **40**, 146–153 (2012); 10.1016/j.jdent.2011.12.006
51. Manicone, P.F., Iommetti, P.R. & Raffaelli, L. An overview of zirconia ceramics: basic properties and clinical applications. *J. Dent.* **35**, 819–826 (2007); 10.1016/j.jdent.2007.07.008
52. Chu, Jia-Hong, Lee, J., Chang, Chun-Chi, Chan, Yu-Chen, Liou, Ming-Li, Lee, Jyh-Wei, Jang, Jason Shian-Ching & Duh, Jenq-Gong. Antimicrobial characteristics in Cu-containing Zr-based thin film metallic glass, *Surface and Coatings Technology* **259**, 87–93 (2014).
53. Secinti, M., Ayten, G., Kahilogullari, G., Kaygusuz, H.C. & Ugur, A. Antibacterial effects of electrically activated vertebral implants. *J. Clin. Neurosci.* **15**, 434–439 (2008).
54. Kaiming Han, Hui Jiang, Yingmin Wang, Jianbing Qiang, Changyang Yu, Antimicrobial Zr-based bulk metallic glasses for surgical devices applications, Journal of Non-Crystalline Solids, Volume 564, 2021.

Figures

Figure 1

Schematic presentation displays the fabrication methods employed in the present study for preparation of $Cu_{50}(Zr_{50-x}Ni_x)$ metallic glass (MG) coated/SUS 304. (**a**) Preparations of MG alloy powders with different Ni concentration, x (x, 10, 20, 30, and 40 at. %) using low energy ball milling technique, and (**b**) coating of SUS 304 substrate with as-prepared MG powders by cold spray approach.

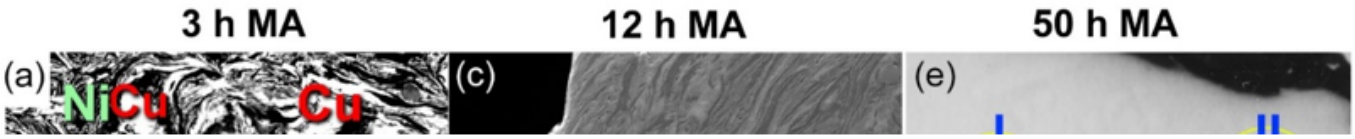

Figure 2

Metallographic characteristics of mechanically alloyed (MA) powders obtained after different stages of ball milling time. The field-emission scanning electron microscope (FE-SEM) images of MA, and $Cu_{50}Zr_{40}Ni_{10}$ powders obtained after 3, 12, and 50 h of low energy ball milling time, are presented in (**a**), (**c**), and (**e**) for $Cu_{50}Zr_{20}Ni_{30}$ system, whereas the corresponding images of the $Cu_{50}Zr_{40}Ni_{10}$ system, taken after the same MA time are displayed in (**b**), (**d**), and (**f**).

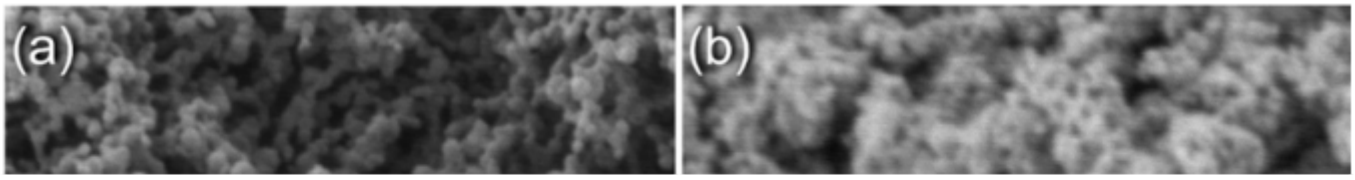

Figure 3

Morphological characteristics of $Cu_{50}(Zr_{50-x}Ni_x)$ powders obtained after 50 h of MA time. The FE-SEM images of the powders obtained after 50 of MA time are shown in (**a**), (**b**), (**c**), and (**d**) for $Cu_{50}Zr_{40}Ni_{10}$, $Cu_{50}Zr_{30}Ni_{20}$, $Cu_{50}Zr_{20}Ni_{30}$, $Cu_{50}Zr_{10}Ni_{40}$ systems, respectively.

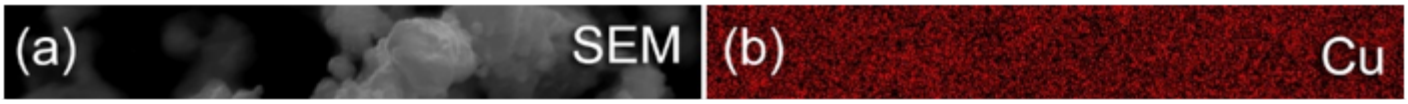

Figure 4

Morphological and local elemental distributions conducted by FE-SEM/ energy dispersive X-ray spectroscopy (EDS) for MG $Cu_{50}Zr_{30}Ni_{20}$ powders obtained after 50 of MA time. (**a**) SEM, and X-ray EDS mapping of (**b**) Cu-K_a, (**c**) Zr-L_a, and (**d**) Ni-K_a images.

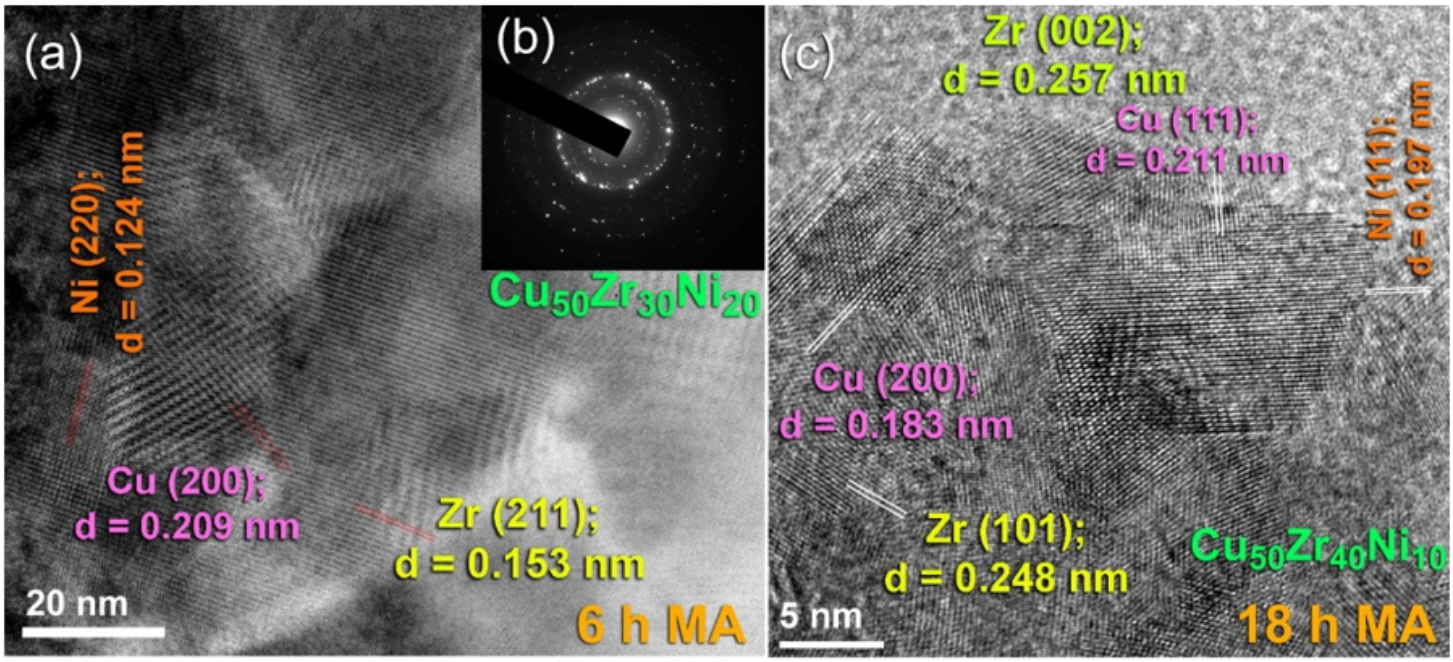

Figure 5

Local structure characteristics of the MA powders obtained after the early (6 h), and intermediate (18 h) stages. (**a**) Field-emission high resolution transmission electron microscope (FE-HRTEM), and (**b**) corresponding selected area diffraction pattern (SADP) of $Cu_{50}Zr_{30}Ni_{20}$ powders after MA for 6 h. The FE-HRTEM image of $Cu_{50}Zr_{40}Ni_{10}$ obtained after 18 h of MA time is displayed in (**c**).

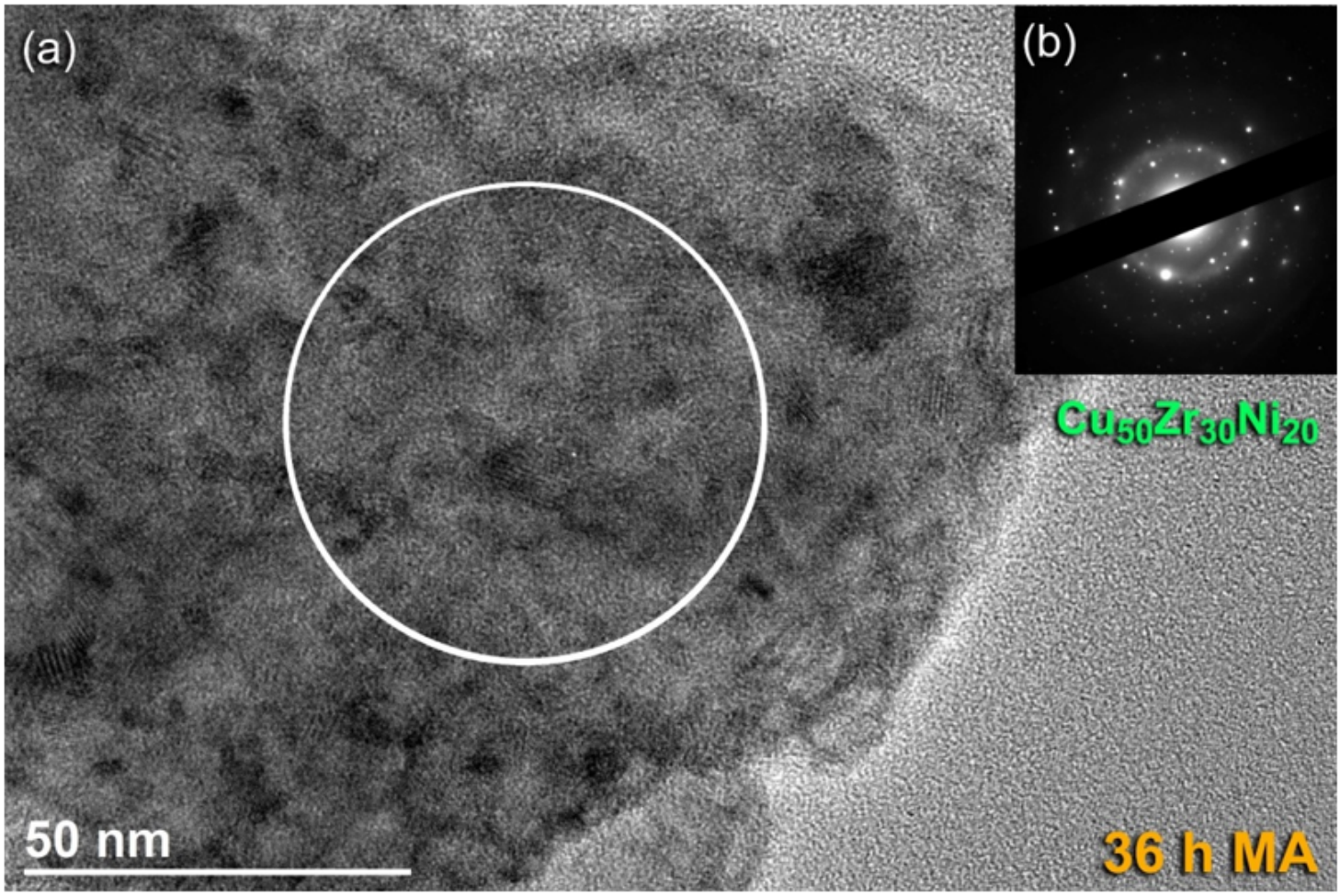

Figure 6

Local structural characteristics beyond the nano-level of 36 h- $Cu_{50}Zr_{30}Ni_{20}$ powders. (**a**) Bright field image (BFI), and corresponding (**b**) SADP of $Cu_{50}Zr_{30}Ni_{20}$ powders obtained after milling for 36 h of MA time.

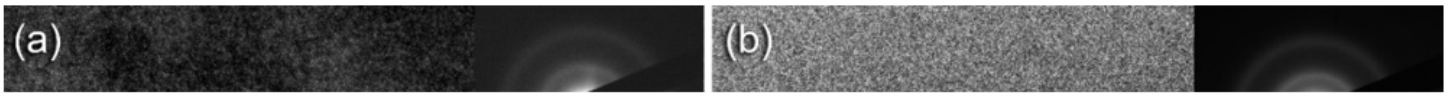

Figure 7

Local structure of the final product of MG $Cu_{50}(Zr_{50-x}Ni_x)$ systems. FE-HRTEM, and related nanobeam diffraction patterns (NBDPs) of (**a**) $Cu_{50}Zr_{40}Ni_{10}$, (**b**) $Cu_{50}Zr_{30}Ni_{20}$, (**c**) $Cu_{50}Zr_{20}Ni_{30}$, and (**d**) $Cu_{50}Zr_{10}Ni_{40}$ obtained after 50 h of MA time.

Figure 8

Thermal stabilities, indexed by glass transition temperature (T_g), crystallization temperature (T_x), supercooled liquid region (DT_x) of $Cu_{50}(Zr_{50-x}Ni_x)$ MG powders obtained after 50 h of MA time. Differential scanning calorimeter (DSC) thermograms of (**a**) $Cu_{50}Zr_{40}Ni_{10}$, (**b**) $Cu_{50}Zr_{30}Ni_{20}$, (**c**) $Cu_{50}Zr_{20}Ni_{30}$, and (**e**) $Cu_{50}Zr_{10}Ni_{40}$ MG alloys powders obtained after 50 h of MA time. The x-ray diffraction (XRD) pattern of $Cu_{50}Zr_{30}Ni_{20}$ sample that was heated in the DSC up to ~ 700 ^{o}C is shown in (**d**).

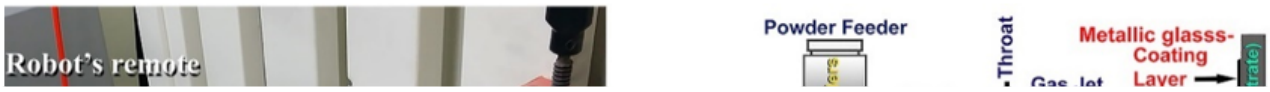

Figure 9

Schematic presentation of the cold spray process, which was employed in the present study for fabrication of MG $Cu_{50}Zr_{20}Ni_{30}$ coated /SUS 304 antibiofilm. (**a**) An onsite photo displays the cold spray coating procedure, (**b**) detailed components and accessories of a modern cold spray equipment, and (**c**) schematic illustration shows the coating procedure, and the deposition mechanism of cold spray MG powders on a SUS 304 surface. The final MG coated/ SUS 304, which was obtained after cold spray at 550 ^{o}C for five continuous times is presented in (**d**).

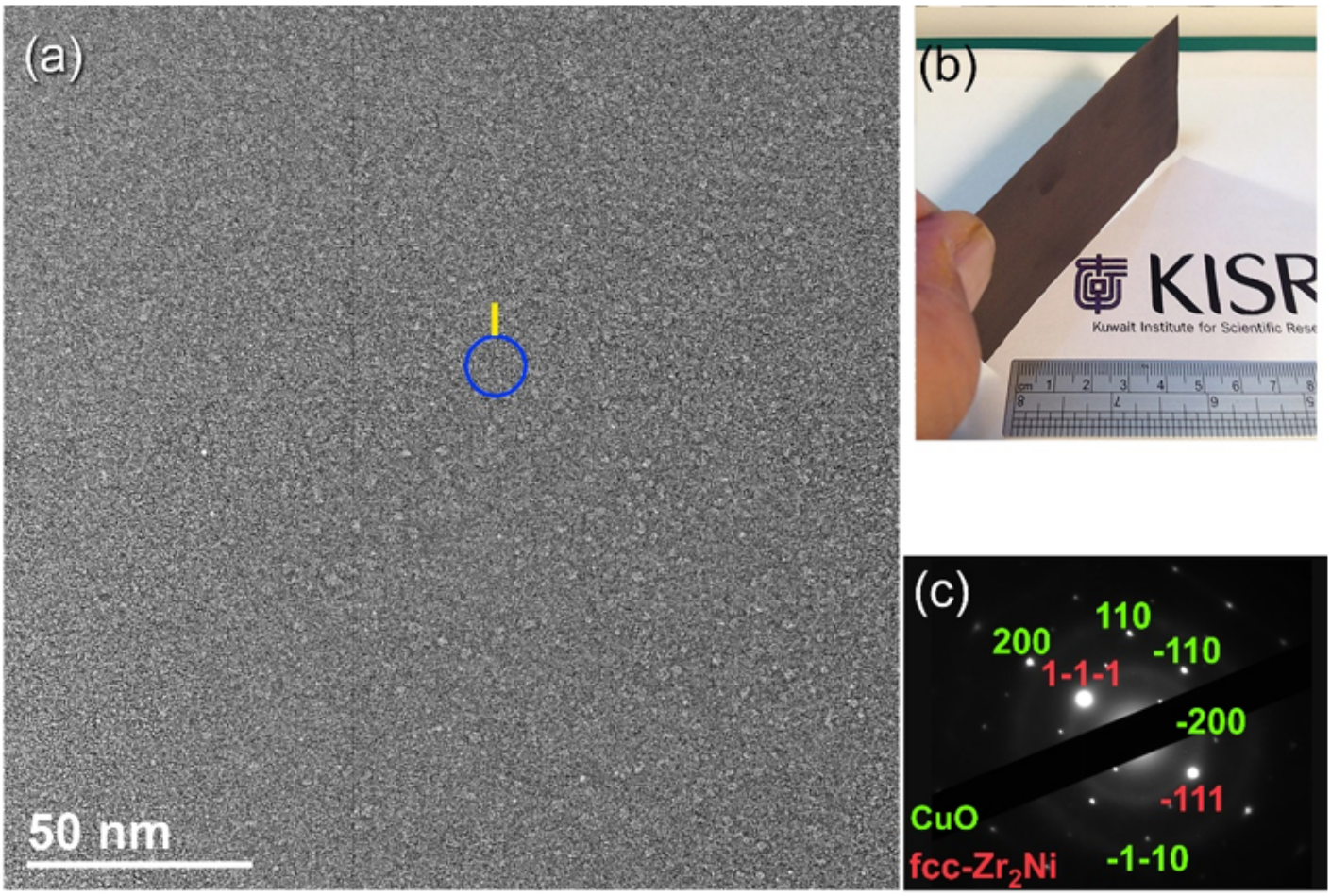

Figure 10

(**a**) FE-HRTEM image of MG powders that were coated on (**b**) SUS 304 substrate (inset of the figure). The indexed NBDP of the circular symbol shown in (**a**) is displayed in (**c**).

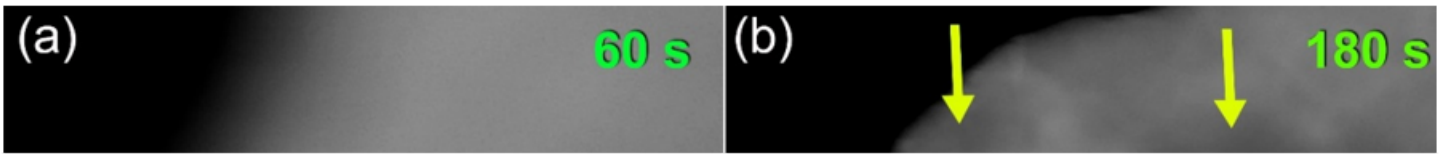

Figure 11

Scanning transmission electron microscope/dark field images (STEM/DFIs) of cold $Cu_{50}Zr_{20}Ni_{30}$ MG powders deposited on SUS 304 ^{o}C for (**a**) 60 s, and (**b**) 180 s. The atomic resolution TEM image, and the related NBDP of the circular symbol indexed in Fig.10a for the powders deposited on the substrate for 1800 s are displayed in (**c**) and (**d**), respectively.

Figure 12

Effect of cold spray on the structure and thermal stability of MG $Cu_{50}Zr_{30}Ni_{20}$ powders. XRD pattern of MG $Cu_{50}Zr_{30}Ni_{20}$ powders obtained after 50 h of MA time are displayed in (**a**). The XRD pattern and corresponding DSC thermogram of the MA powders that were cold spray at 550 ^{o}C are displayed in (**b**) and (**c**), respectively. The XRD patterns of the cold sprayed MG powders heated up to 600 ^{o}C, and 700 ^{o}C, are displayed in (**d**) and (**e**), respectively.

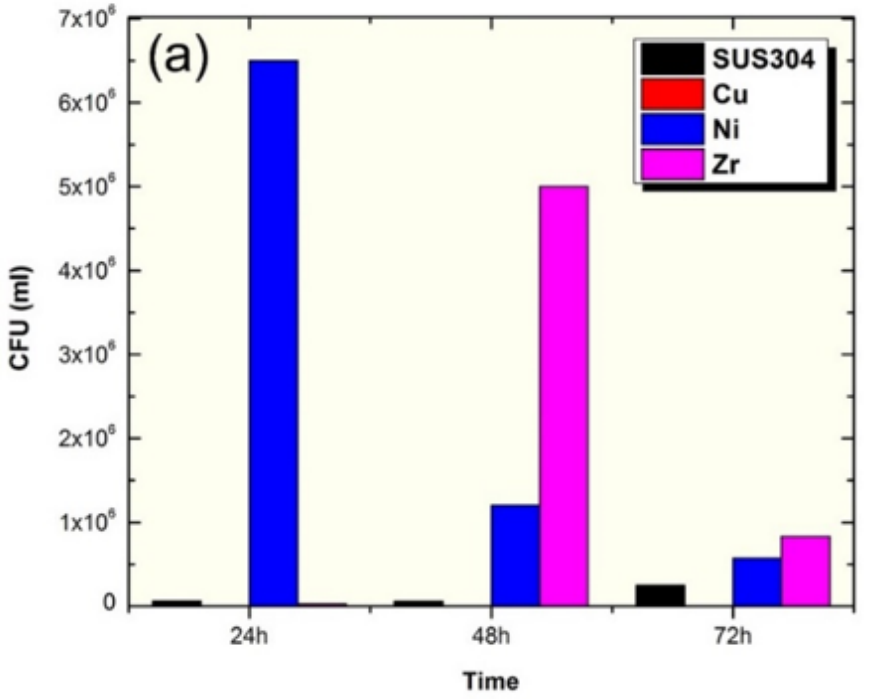

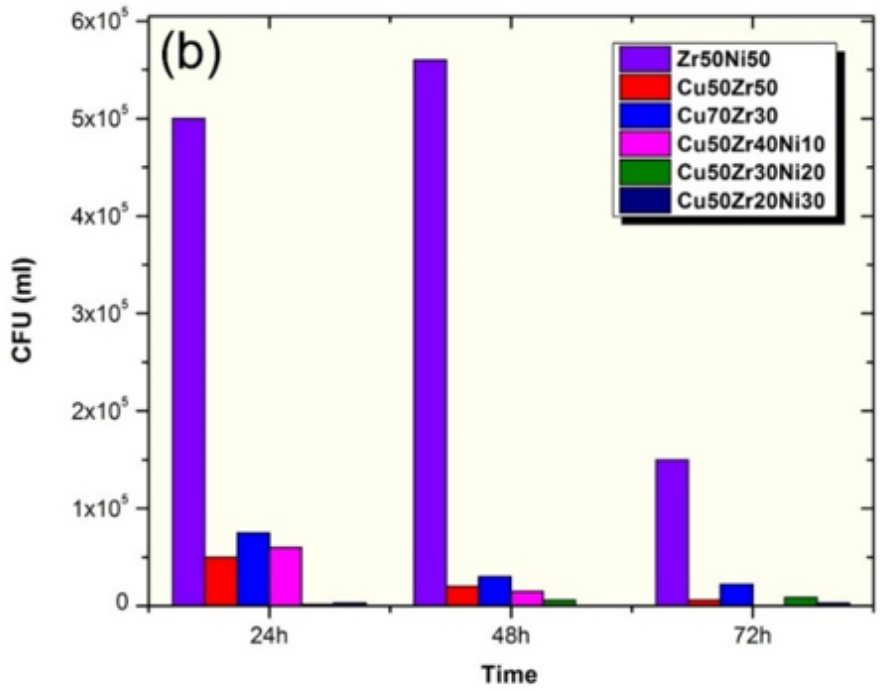

Figure 13

Inhibition of biofilm adhesion on (**a**) uncoated SUS304 coupons, and elemental Cu, Ni, and Zr metals, (**b**) binary $Zr_{50}Ni_{50}$, $Cu_{50}Zr_{50}$, and $Cu_{70}Zr_{30}$ systems. The results for inhibition of biofilm adhesion of selected ternary $Cu_{50}(Zr_{50-x}Ni_x)$ systems (x, 10, 20, 30 at.%) are displayed in (**b**). E.coli (ATCC 25922) biofilm viable counts were enumerated at different time points (24, 48 and 72 h) from tested coating alloy (13b) or control coated and non-coated coupons (13a). Biofilm formed by E.coli (ATCC 25922) was significantly inhibited by ternary systems (CuZrNi) at all times points tested in comparison to control coated coupons. Results represents mean ± SD of 3 independent experiments.

Supplementary Files

This is a list of supplementary files associated with this preprint. Click to download.

- GA.png